DOI: https://doi.org/10.15517/3fczkg02

# TRANSPARENT SPHERES AS GRAVITATIONAL LENSES

# ESFERAS TRANSPARENTES COMO LENTES GRAVITACIONALES

EDWIN SANTIAGO-LEANDRO $^1$  ALEXANDER MORA-CHAVERRI $^2$ 

FRANCISCO FRUTOS-ALFARO $^3$ 

Received: 29/Ago/2023; Accepted: 29/May/2025

Revista de Matemática: Teoría y Aplicaciones is licensed under a Creative Commons Reconocimiento-NoComercial-Compartirigual 4.0 International License. Creado a partir de la obra en http://www.revistas.ucr.ac.cr/index.php/matematica



 $<sup>^1</sup>$  Universidad de Costa Rica, Centro de Investigaciones Espaciales, San José, Costa Rica. E-Mail: <code>esantiago@inaoep.mx</code>

<sup>&</sup>lt;sup>2</sup> Universidad de Costa Rica, Centro de Investigaciones Espaciales, San José, Costa Rica. E-Mail: alexander.morachaverri@ucr.ac.cr

<sup>&</sup>lt;sup>3</sup> Universidad de Costa Rica, Centro de Investigaciones Espaciales, San José, Costa Rica. E-Mail: francisco.frutos@ucr.ac.cr

#### Abstract

In this work, we present a concise and educational study of gravitational lensing by transparent matter distributions. We focus on the calculation of image properties for several idealized mass profiles, including the uniform transparent sphere, the isothermal gas sphere, the non singular isothermal sphere, and the transparent King profile. Using numerical techniques and the XFGLenses software, we compute and visualize the resulting lensed images, along with the associated critical curves and caustics. The results are consistent with established theoretical predictions for transparent lenses, for example, the occurrence of an odd number of images, and the reduction of two images as the source crosses a caustic. The caustic geometries observed include diamond-shaped, elliptical, and lemniscate-like structures. Among the critical curves, ellipses were most commonly observed, while lemniscate-like forms emerged specifically in the transparent non-singular isothermal sphere case, in agreement with known behaviors in gravitational lensing by smooth matter distributions.

Keywords: gravitational lensing; numerical simulations; general relativity.

#### Resumen

En esta contribución, presentamos un estudio conciso y educativo de lentes gravitacionales debido a distribuciones de masa transparentes. Nos enfocamos en los cálculos de las propiedades de la imagen para perfiles de masa idealizados, incluyendo la esfera transparente uniforme, la esfera de gas isotérmico, la esfera de gas isotérmico no singular, y el perfil de King transparente. Utilizando técnicas numéricas y el software XFGLenses, se calculan y se visualizan las imágenes resultantes, junto con las curvas críticas y cáusticas asociadas. Los resultados son consistentes con las predicciones teóricas de los lentes transparentes, como lo son un número impar de imágenes, y la reducción del número de imágenes en dos cuando la fuente atraviesa la cáustica. Las geometrías que presentan las curvas cáusticas encontradas incluyen la forma de diamante, forma elíptica, y tipo lemniscata. Entre las curvas críticas, formas elípticas fueron las más encontradas, y la forma tipo lemniscata aparecieron específicamente en el case de la esfera isotérmica no singular, lo cual es esperado de lo conocido de lentes gravitacionales debido a distribuciones ideales.

Palabras clave: lentes gravitacionales; simulaciones numéricas; relatividad general.

Mathematics Subject Classification: Primary: 83-01, 83-08; secondary 85-04, 97Mxx.

## 1. Introduction

Due to the curvature of space-time, light rays from a distant source can take different paths in the presence of a massive object. In this way, multiple images can be generated due to this effect. The mass distribution of the lens plays an important role in the generation of these images. This phenomenon of observing multiple

images is called gravitational lensing [30]. Gravitational lenses were proposed by several researchers since Einstein's time, including Einstein himself [29]. However, these objects were not observed until 1979 [37]. After this discovery, observations increased and currently more than 100 gravitational lenses have been observed over multiple wavebands (See [17, 28, 32]). With the release of projects like the James Webb Space Telescope, and the Rubin Observatory Legacy Survey of Space and Time, the interest in strong gravitational lenses has once again increased dramatically [34, 36]. It has even been claimed that a strong gravitational lens could improve the angular resolution of modern gamma-ray instruments up to 6 orders of magnitude [2].

The treatment of gravitational lenses as transparent objects has not been considered as much as the opaque case, but some interesting studies have appeared throughout the years. In 1971, Clark considered the uniform and transparent gravitational lens and calculated the deflection angle and the effects on beam area, apparent luminosity and focusing effects [7]. Bourassa and Kantowski made further calculations on cases with spheroidal symmetry [3, 4]. After this, in 1984, there was a minor correction made by Bray in the surface density integral made by Bourassa and Kantowski [5]. Another article regarding the subject was made by McKenzie in 1985, where he shows that transparent lenses make an odd number of images [24]. This was also shown by Dyer and Roeder in 1980 [9]. Although Gottlieb argues this is not always true [13]. Nandor and Helliwell analyzed gravitational lensing with Fermat's principle and they used the model of a transparent lens with a logarithmic varying thickness [25]. Fermat's principle in the study of strong gravitational lenses has also appeared more recently in 2013 [18], and in 2014 an interesting software named GLASS appeared to help figure out gravitational lens models from observational data [8]. Another use of the transparent case was done by Patla and Nemiroff in 2008, where they modelled the Sun as a Transparent Sphere [27]. Theoretical work in gravitational lensing nowadays is more focused on exploring gravitational lensing under new metrics, multiplane sources, or even developing the analysis through geometric optics [33].

There have also been interesting experiments where images with transparent objects were reproduced, simulating the effects realistically. In 1969, Liebes used Plexiglas to simulate magnification and lensing effects like the ones he studied previously in 1964 [22, 23]. Icke constructed a cylindrical lens, also employing Plexiglas, to approximate the lensing of a point mass object in 1980 [16]. Higbie used Plexiglass too [14], and Falbo-Kenkel and Lohre used bases of wine glasses to simulate gravitational lensing [10]. Adler et al. employed plastic lenses according to their calculations for the point mass, the constant density sphere and the isothermal gas sphere [1]. Recently, Selmke used a setup with a water filled acrylic pool and small discs to replicate the case of a single, a binary and a triple mass lens [31]. There is even an interesting work from 2022 where Xu et al. try to model gravitational lensing effects with metamaterial in a thin elastic plate [38]. That said, not much has been done in terms of computer simulations of these images caused by the transparent cases. There have been works such as Newbury and Spi-

teri in 2002 [26], but the focus is not in the transparent case nor in the macrolens generalization (See Section 2.2). It is unsurprising that not much attention has been given to this aspect of gravitational lensing now that the community has focused on other aspects of the theory. Moreover, we consider an interesting avenue for educational purposes on bringing back attention to the computational modeling of the images that has been relatively unexplored, as opposed to exploring the concepts through experiments.

In gravitational lensing, the singular isothermal sphere (SIS) represents a simplified mass distribution where the mass density decreases as the inverse square of the distance from the center (leading to a singularity at the center). This model is useful because it provides a good approximation for the mass distribution of certain types of galaxy clusters or elliptical galaxies. The SIS model helps in understanding how light from a background object is bent around a foreground mass, causing the characteristic lensing effects such as multiple images or distorted arcs [35].

The Non-Singular Isothermal Sphere (NIS) model is another variant used in gravitational lensing studies, and it serves as an extension or refinement of the SIS model. Unlike the SIS model, the NIS model modifies this approach to avoid the singularity. This model helps in overcoming the limitations of the SIS model by providing a more physically plausible description of a mass distribution, particularly in systems where the core density needs to be finite [15].

The King model profile is valuable for modeling systems with a finite extent and a well-defined core, making it useful for both stellar clusters and certain types of galaxy clusters in gravitational lensing studies [39]. In this article we review these gravitational lens models.

Adler et al. calculated the deflection angle for the transparent uniform sphere, the transparent SIS, and the non-singular case (NIS) [1]. In this article, using the results of Adler et al., we develop and get the calculations that are necessary to plot the caustics and critical curves. The transparent King profile, and its derivatives are also included. From these results, images are obtained for the different transparent profiles, with some caustics and critical curves associated with these profiles. Although we do this mainly for educational purposes, considering that the concepts of strong gravitational lensing are well represented in the models we studied, we also consider valuable for these calculations and images to be in the contribution, given that this area is relatively unexplored. For the computational images, the simulator XFGLenses [11, 12] is employed and for some of the critical curves and caustics, and a code made in MATLAB is used to find the curves. XGFLenses is a computational tool capable of producing the images that produces a certain galaxy or galaxy cluster given the density distribution and the parameters relevant for the calculation of the images. It is also capable of calculating the caustics of a given gravitational lens. Our aim is to better illustrate the strong gravitational lensing by transparent matter distribution concepts by making computer simulated images made with XFGLenses of different transparent cases, including the transparent and uniform sphere, and the non uniform cases with spheroidal symmetry. It is important to note that we want this article to serve as an introduction for someone interested in the topic, alongside some findings regarding the differences between images, caustic and critic curves for different density profiles in the transparent sphere and adding macrolenses, with the aid of computational simulations.

The structure of the paper is as follows: in Section 2, a brief description of the gravitational lens theory is given. In Section 3, the transparent uniform sphere is discussed. In following sections, the results for the mentioned lens models are presented. In Section 7, we will show the images and analyze them, and in Section 8, some conclusions are given.

#### 2. Gravitational lenses

## 2.1. Deflection angle.

For the case of a point mass, using the Schwarzschild metric, it can be shown from the geodesic equation that the deflection angle, is given by

$$\hat{\alpha} = \frac{4GM}{c^2 \xi},\tag{2.1}$$

where  $\hat{\alpha}$  is the deflection angle (See Figure 1), G is the gravitational constant, M is the mass of the deflecting object, c is the speed of light and  $\xi$  is the impact parameter or the closest distance from the light to the object. This is valid for small angles of deflection [30].

Starting from a point mass distribution, it is possible to generalize the previous result to a mass distribution by integrating Equation 2.1, obtaining

$$\hat{\alpha}(\boldsymbol{\xi}) = \frac{4G}{c^2} \int_{\mathbb{R}^2} \Sigma(\boldsymbol{\xi}') \frac{(\boldsymbol{\xi} - \boldsymbol{\xi}')}{|\boldsymbol{\xi} - \boldsymbol{\xi}'|^2} d^2 \boldsymbol{\xi}', \tag{2.2}$$

where  $\Sigma(\xi')$  is the surface mass distribution, and we are using bold characters to represent vectors and matrices. Even though it is clear that the mass distribution is a volumetric distribution, we can use the fact that the size of the lens is very small compared to the cosmological distances from the lens to the source plane and to the observer. This is known as the *thin lens approximation*.

In this article, we calculate different deflection angles but in all cases the matter distributions are axially symmetric. This allows the deflection angle equation to be reduced to a similar form according to Equation 2.1, as follows:

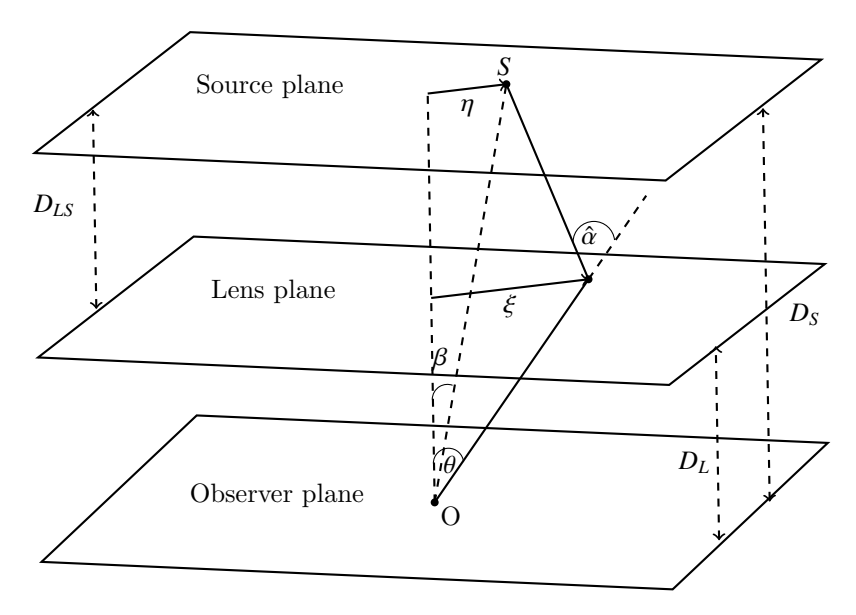


**Figure 1:** Diagram of the angle of deflection, showing the plane of the Source, the plane where the lens is located, and the plane of the observer.

$$\hat{\alpha}(r) = \frac{4GM(r)}{c^2 r},\tag{2.3}$$

where M(r) is the projected mass that is enclosed a distance r from the origin (See Figure 2). This simplifies the procedure of obtaining the angle of deflection by just calculating M(r) for a given distribution. There are actually two ways of calculating M(r). For a tridimensional mass distribution  $\mu(r)$ , one can calculate the projected bidimensional distribution  $\Sigma(\xi)$  by applying an Abel Transformation [19] to find M(r), or, alternatively, one can perform the tridimensional integration with  $\mu(r)$ , making sure that the integration only encompasses the enclosed mass in a cylinder of radius r as seen from Earth (see Figure 2).

### 2.2. Lens equation.

Although gravitational lensing is an effect from general relativity, it is possible to establish a purely geometric relation. Using the notation from Figure 1, the following geometric relation can be written as

$$\beta = \theta - \frac{D_{LS}}{D_S} \hat{\alpha}, \tag{2.4}$$

where  $\beta$  is the angle the observer and the source make with a line normal to the lens plane,  $\theta$  is the angle between a line normal to the lens plane and the ray of

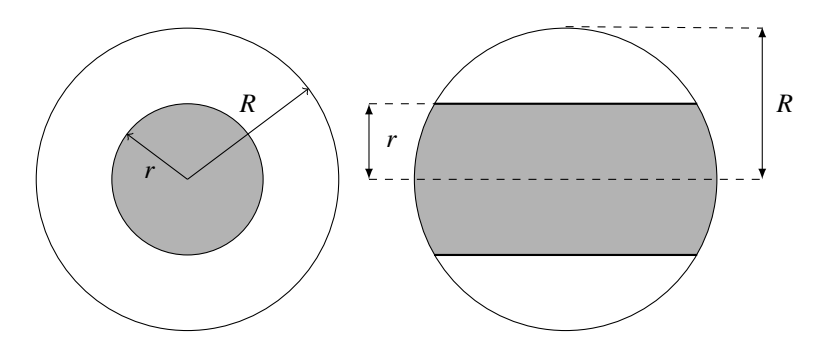


Figure 2: Diagram of the enclosed mass in a cylinder of radius r. The left image represents the projected mass, as seen from Earth. On the right, the lateral view.

light before deflection,  $D_L$  is the distance between the Observer plane and the Lens plane,  $D_{LS}$  is the distance between the Source plane and the Lens plane, and  $D_S$  is the distance between the Observer plane and the Source plane (in cosmology, distances cannot be added:  $D_S \neq D_L + D_{LS}$ . If the reader is interested in how to work with cosmological distances, we recommend the work from Kayser in 1997 [20]). From (2.4), the dimensionless lens equation

$$y = x - \alpha(x), \tag{2.5}$$

is obtained, where

$$\alpha(\mathbf{x}) = \frac{D_L D_{LS}}{\xi_0 D_S} \hat{\alpha}(\xi_0 \mathbf{x}) = \int_{\mathbb{R}^2} \kappa(\mathbf{x}') \frac{(\mathbf{x} - \mathbf{x}')}{|\mathbf{x} - \mathbf{x}'|^2} d^2 \mathbf{x}',$$
$$\mathbf{y} \equiv \frac{\eta}{\eta_0} \quad \text{and} \quad \mathbf{x} \equiv \frac{\xi}{\xi_0}.$$

The parameter  $\xi_0$  is the length scale on the lens surface. The dimensionless surface density of the lens is given by

$$\kappa(\mathbf{x}) = \frac{\Sigma(\boldsymbol{\xi})}{\Sigma_c},\tag{2.6}$$

where  $\Sigma_c$  represents the critical density, which is given by

$$\Sigma_c = \frac{c^2 D_S}{4\pi G D_L D_{LS}}. (2.7)$$

A generalization of the lens equation (2.5) is

$$y = M \cdot x - \alpha(x), \tag{2.8}$$

where  $\mathbf{x} = (x_1, x_2)^T$  is the image position on the lens plane  $(x^2 = x_1^2 + x_2^2), \mathbf{y} = (y_1, y_2)^T$  is the source position on the source plane, and the matrix  $\mathbf{M}$  is given by

$$\mathbf{M} = \begin{pmatrix} 1 - \sigma - \gamma \cos 2\phi & -\gamma \sin 2\phi \\ -\gamma \sin 2\phi & 1 - \sigma + \gamma \cos 2\phi \end{pmatrix}, \tag{2.9}$$

where  $\sigma$  is the dimensionless macrolens density,  $\gamma$  is the dimensionless macrolens shear, and  $\phi$  is the shear angle. In a physical sense,  $\sigma$  can contribute to the magnification or reduction of the lens,  $\gamma$  to the deformation of the lens, and  $\phi$  to a rotation in the lens. Notice that when all of these 3 quantities are 0, M becomes the identity matrix and Equation 2.8 reduces to Equation 2.5. The components  $M_{ij}$  (i, j = 1, 2) of the matrix are:

$$M_{11} = 1 - \sigma - \gamma \cos 2\phi,$$
  
 $M_{12} = M_{21} = -\gamma \sin 2\phi,$  (2.10)  
 $M_{22} = 1 - \sigma + \gamma \cos 2\phi.$ 

### 2.3. Caustics and critical curves.

The critical and caustic curves are important in gravitational lensing analysis, because they divide the lens into regions of interest. Knowing the caustics and the position of the source, the number of images that a gravitational lens will create can be determined, as well as where the images will be magnified [30].

The critical curves are the curves that are formed in the lens plane, on the other hand, the caustics are formed in the source plane. It can be shown that the magnification of a gravitational lens is inversely proportional to the determinant of the Jacobian matrix. Because the caustic gives us information about the concentration of light rays, mathematically the curve we are looking for can be found when the magnification diverges [30]. Thus, critical curves can be obtained if the determinant of the Jacobian is equal to zero, that is  $\det(J) = 0$  with the matrix J given by

$$\boldsymbol{J} = \begin{pmatrix} J_{11} & J_{12} \\ J_{21} & J_{22} \end{pmatrix} = \frac{\partial \boldsymbol{y}}{\partial \boldsymbol{x}},$$

were the components of J are:

$$J_{11} = \frac{\partial y_1}{\partial x_1} = \left( M_{11} - \frac{\alpha}{x} \right) - \frac{x_1^2}{x^2} \left( \frac{d\alpha}{dx} - \frac{\alpha}{x} \right),$$

$$J_{12} = \frac{\partial y_1}{\partial x_2} = M_{12} - \frac{x_1 x_2}{x^2} \left( \frac{d\alpha}{dx} - \frac{\alpha}{x} \right),$$

$$J_{21} = \frac{\partial y_2}{\partial x_1} = M_{21} - \frac{x_1 x_2}{x^2} \left( \frac{d\alpha}{dx} - \frac{\alpha}{x} \right),$$

$$J_{22} = \frac{\partial y_2}{\partial x_2} = \left( M_{22} - \frac{\alpha}{x} \right) - \frac{x_2^2}{x^2} \left( \frac{d\alpha}{dx} - \frac{\alpha}{x} \right).$$

$$(2.11)$$

Then, the determinant of the Jacobian is given by

$$\mathcal{J} = \det \mathbf{J} = J_{11}J_{22} - J_{12}J_{21}$$

$$= \left[ \left( M_{11} - x_2^2 \frac{\alpha}{x^3} \right) - \frac{x_1^2}{x^2} \frac{d\alpha}{dx} \right]$$

$$\times \left[ \left( M_{22} - x_1^2 \frac{\alpha}{x^3} \right) - \frac{x_2^2}{x^2} \frac{d\alpha}{dx} \right]$$

$$- \left[ M_{12} - \frac{x_1 x_2}{x^2} \left( \frac{d\alpha}{dx} - \frac{\alpha}{x} \right) \right]$$

$$\times \left[ M_{12} - \frac{x_1 x_2}{x^2} \left( \frac{d\alpha}{dx} - \frac{\alpha}{x} \right) \right].$$
(2.12)

The caustics are mapped using the lens equation, in which the  $x_1$  and  $x_2$  are evaluated by equating the determinant of the Jacobian matrix to zero. Caustic curves are generally described by polar curves, therefore using the following change of variable of  $x_1$  and  $x_2$  in terms of  $\theta$  and  $x_3$ :

$$x_1 = x \cos \theta,$$
  

$$x_2 = x \sin \theta.$$
 (2.13)

From (2.8), (2.10) and (2.11), we can obtain a general expression for the determinant given by

$$\det \mathbf{J} = \det \mathbf{M} + \left(\frac{d\alpha}{dx} - \operatorname{Tr} \mathbf{M}\right) \frac{\alpha}{x} - \left(\frac{d\alpha}{dx} - \frac{\alpha}{x}\right) \left(\frac{1}{2}\operatorname{Tr} \mathbf{M} + \gamma \cos(2(\theta - \phi))\right). \tag{2.14}$$

Considering the case in which M is equal to identity matrix, Equation (2.14) does not depend on the angular coordinate ( $\gamma = 0$ ), reducing to the expression

$$\det \mathbf{J} = \left(\frac{\alpha}{x} - 1\right) \left(\frac{d\alpha}{dx} - 1\right). \tag{2.15}$$

In this case, the form of the caustics can be obtained from

$$\left(\frac{d\alpha}{dx} - 1\right)\left(\frac{\alpha}{x} - 1\right) = 0. \tag{2.16}$$

### 3. Transparent Sphere

As first example, the transparent sphere is considered. Whether it is the transparent or opaque case, an uniform matter distribution is useful as a first case to study, because it is among the easiest mass distributions.

The transparent sphere density is given by

$$\mu(r) = \begin{cases} M/V & r \le R, \\ 0 & r > R, \end{cases}$$
 (3.1)

where M is its mass, R its radius, and  $V = 4\pi R^3/3$  its volume. Because the transparent uniform sphere is axially symmetric, we only need to pay attention to the enclosed mass a distance r from the center of the distribution, so it can be scaled to find the deflection angle as a function of the scaled radius x.

The integration for M(r) gives

$$M(r) = 4\pi \int_0^r \int_0^{\sqrt{R^2 - \rho^2}} \mu \rho dz d\rho = M \left[ 1 - \left( 1 - \frac{r^2}{R^2} \right)^{3/2} \right]. \tag{3.2}$$

Then, the deflection angle would be

$$\alpha = \frac{2R_s}{r} \left[ 1 - \left( 1 - \frac{r^2}{R^2} \right)^{3/2} \right],\tag{3.3}$$

where  $R_s = 2GM/c^2$  is the Schwarzschild radius. The final step is to scale in terms of x. The way this is done is by defining  $x = r/(2R_s)$ , and  $x_0 = R/(2R_s)$ , where x,  $x_0$  are the new scaled variable and the new scaled radius, respectively. From this, the Einstein angle becomes

$$\alpha(x) = \begin{cases} \frac{1}{x} \left[ 1 - \left( 1 - \frac{x^2}{x_0^2} \right)^{3/2} \right] & x \le x_0, \\ \frac{1}{x} & x > x_0. \end{cases}$$
 (3.4)

The derivative is

$$\frac{d\alpha}{dx} = \begin{cases} -f(x) & x \le x_0, \\ -\frac{1}{x^2} & x > x_0, \end{cases}$$
 (3.5)

with

$$f(x) = \frac{1}{x^2} \left[ 1 - \left( 1 - \frac{x^2}{x_0^2} \right)^{3/2} \right] - \frac{3}{x_0^2} \left( 1 - \frac{x^2}{x_0^2} \right)^{1/2}.$$
 (3.6)

## 4. Transparent Isothermal Gas Sphere

The singular isothermal gas sphere or SIS describes a relatively simple distribution of matter with certain realistic properties. It is an axially symmetric distribution that gives flat rotation curves. This is important to describe the dark matter halo in galaxies. The name stems from the fact that it also represents a distribution of gas where the pressure is proportional to its density [1, 30].

The density profile for the SIS is

$$\mu(r) = \frac{b}{r^2} = \frac{b}{\rho^2 + z^2},\tag{4.1}$$

where b is a parameter of the model that is fitted according to the distribution in question. Here, the deflection angle becomes [1]

$$\hat{\alpha}(r) = \frac{2R_s}{r} \left[ 1 - \left( 1 - \frac{r^2}{R^2} \right)^{\frac{1}{2}} + \frac{r}{R} \arccos\left(\frac{r}{R}\right) \right],\tag{4.2}$$

with total mass  $M=4\pi bR$ . Now, the scaled deflection angle is

$$\alpha(x) = \frac{1}{x} \left[ 1 - \left( 1 - \frac{x^2}{x_0^2} \right)^{\frac{1}{2}} + \frac{x}{x_0} \arccos\left(\frac{x}{x_0}\right) \right]. \tag{4.3}$$

The derivative of the deflection angle is

$$\frac{d\alpha}{dx} = \frac{-1}{x^2} \left[ 1 - \left( 1 - \frac{x^2}{x_0^2} \right)^{\frac{1}{2}} \right]. \tag{4.4}$$

## 5. Transparent non Singular Isothermal Gas Sphere

The non Singular Isothermal Gas Sphere (NIS) generalizes the SIS by adding a core radius, which eliminates the divergence the SIS model has at r = 0. Moreover, this model is more studied because realistic mass distributions and gravitational lenses are better reproduced with a non singular model, when compared to a singular one. For the NIS distribution, the density profile is given by

$$\mu(\rho, z) = \frac{b}{\rho^2 + z^2 + r_c^2},\tag{5.1}$$

where  $r_c$  is the core radius. The deflection angle is [1]

$$\hat{\alpha}(r) = \frac{2R_s}{r\beta_3} \left[ 1 - \left( 1 - \frac{r^2}{R^2} \right)^{\frac{1}{2}} + \frac{\sqrt{r^2 + r_c^2}}{R} \arccos \beta_1 - \frac{r_c}{R} \arccos \beta_2 \right]. \tag{5.2}$$

Scaling, the deflection angle becomes

$$\alpha(x) = \frac{1}{x\beta_3} \left[ 1 - \left( 1 - \frac{x^2}{x_0^2} \right)^{\frac{1}{2}} + \frac{\sqrt{x^2 + x_c^2}}{x_0} \arccos \beta_1 - \frac{x_c}{x_0} \arccos \beta_2 \right], \tag{5.3}$$

where

$$x_{c} = r_{c}/(2R_{s}),$$

$$\beta_{1} = \sqrt{\frac{x^{2} + x_{c}^{2}}{x_{0}^{2} + x_{c}^{2}}},$$

$$\beta_{2} = \frac{x_{c}}{\sqrt{x_{0}^{2} + x_{c}^{2}}},$$

$$\beta_{3} = 1 - \frac{x_{c}}{x_{0}}\arccos\beta_{2}.$$
(5.4)

Note that if  $x_c = 0$ , the deflection angle is the SIS angle. Its derivative is

$$\frac{d\alpha}{dx} = \frac{1}{x^2 \beta_3} \left[ \frac{x^2}{x_0 f_1} \arccos \beta_1 + \frac{x^2}{x_0^2 f_0} + f_0 - \frac{x^2}{x_0 f_2 f_3} - \frac{f_1}{x_0} \arccos \beta_1 - \beta_3 \right],\tag{5.5}$$

where

$$f_{0} = \sqrt{1 - \frac{x^{2}}{x_{0}^{2}}},$$

$$f_{1} = \sqrt{x^{2} + x_{c}^{2}},$$

$$f_{2} = \sqrt{x_{0}^{2} + x_{c}^{2}},$$

$$f_{3} = \sqrt{1 - \frac{x^{2} + x_{c}^{2}}{f_{2}^{2}}}.$$

$$(5.6)$$

### 6. Transparent King Model

The King density model was proposed as a distribution that maps the density profile of the Coma cluster of galaxies [21]. Moreover, it is advantageous, because it does not diverge at r=0, and it works well in general as a density model for clusters of galaxies with a flat rotation curve. The King density model is given by [21]

$$\mu(r') = \frac{\mu_0}{(r'^2 + 1)^{\frac{3}{2}}} \,, \tag{6.1}$$

where  $r' = (\rho^2 + z^2)/r_c$  is the scaled distance from the center and  $\rho$  and z are the cylindrical coordinates.

The deflection angle becomes

$$\hat{\alpha}(r) = \frac{16\pi G \mu_0 r_c^3}{c^2 r} \left[ \frac{1}{\sqrt{r_c^2 + R^2}} \left( \sqrt{R^2 - r^2} - R \right) \operatorname{arctanh} \left( \frac{R}{\sqrt{r_c^2 + R^2}} \right) - \operatorname{arctanh} \left( \frac{\sqrt{R^2 - r^2}}{\sqrt{r_c^2 + R^2}} \right) \right]. \tag{6.2}$$

By evaluating to find the total enclosed mass M(r) in r = R, one obtains

$$M = \pi \mu_0 r_c^3 f_4, \tag{6.3}$$

where

$$f_4 = 4 \operatorname{arctanh}\left(\frac{R}{\sqrt{r_c^2 + R^2}}\right) - \frac{R}{\sqrt{r_c^2 + R^2}}.$$
 (6.4)

With this definition, we can write the deflection angle as

$$\hat{\alpha}(r) = \frac{2R_s}{r} \left[ 1 + \frac{1}{f_4} \sqrt{\frac{R^2 - r^2}{r_c^2 + R^2}} - \frac{1}{f_4} \operatorname{arctanh} \left( \sqrt{\frac{R^2 - r^2}{r_c^2 + R^2}} \right) \right]. \tag{6.5}$$

Scaling, and using the definitions  $f_i$  defined for the NIS case, we obtain

$$\alpha(x) = \frac{1}{x} \left[ 1 + \frac{x_0 f_0}{f_5} - \frac{f_2}{f_5} \operatorname{arctanh} \left( \frac{x_0 f_0}{f_2} \right) \right], \tag{6.6}$$

where

$$f_5 = f_2 \operatorname{arctanh}\left(\frac{x_0}{f_2}\right) - x_0. \tag{6.7}$$

The derivative of the deflection angle is

$$\frac{d\alpha}{dx} = -\frac{1}{x^2} \left[ 1 - \frac{f_2^2 x^2}{x_0 f_0 f_5 (f_2^2 - x_0^2 f_0^2)} + \frac{x^2}{x_0 f_0 f_5} - \frac{f_2}{f_5} \operatorname{arctanh} \left( \frac{x_0 f_0}{f_2} \right) + \frac{x_0 f_0}{f_5} \right]. \tag{6.8}$$

## 7. IMAGES, CAUSTICS AND CRITICAL CURVES FOR THE PROFILES

Now, we proceed to analyze the images, caustics and critical curves generated by the profiles described above. Figures 3, 5, 7, 9 and 11 were generated with XFGLenses. For Figures 4, 6, 8, 10 and 12, MATLAB was employed, because the caustics and critical curves for the transparent version of these profiles are not implemented in XFGLenses yet. In Figure 3, a ring is formed if the source is projected at the center of the mass distribution with the parameters  $\gamma$  and  $\sigma$  are null. This is known in gravitational lens theory as an Einstein Ring <sup>1</sup> [30]. Note that the first image in Figure 5 also has the source in the origin. The difference between this image and the one from Figure 3 is that a non-zero value for  $\sigma$  and  $\gamma$  is added. The images are still connected but one can still note that there are four distinct images surrounding the origin and a small image in the origin, having five images in total. This is expected because, as we mentioned in the introduction, a transparent lens should have an odd number of images [24].

<sup>&</sup>lt;sup>1</sup>In fact, Chwolson was the first to publish that a ring could form if the lens, the source and the observer are in the same line of vision. [6]

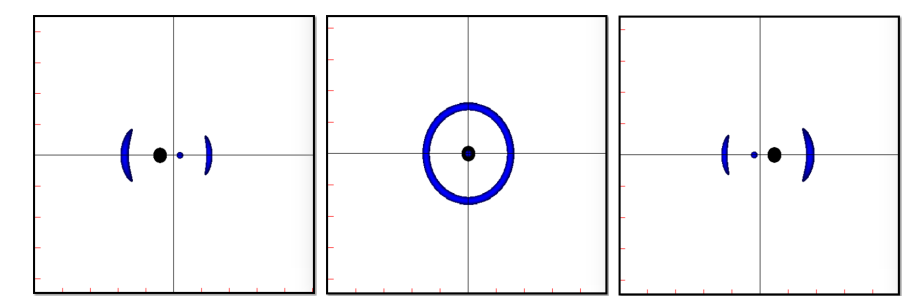


Figure 3: Images for the uniform transparent sphere. The black dot represents where the original source is with respect to the center of the distribution. The values for the parameters ( $\sigma$  and  $\gamma$ ) are null, which means that M = I.

The positions of the caustics of the uniform transparent sphere for M = I(identity matrix) are calculated. Following from (2.14), and using (3.4) and (3.5), we have two equations when  $x < x_0$  that give possible critical curves:

$$1 - \left(1 - \frac{x^2}{x_0^2}\right)^{\frac{3}{2}} - x^2 = 0, (7.1)$$

$$\frac{3}{x_0^2} \left( 1 - \frac{x^2}{x_0^2} \right)^{\frac{1}{2}} - \frac{1}{x^2} \left[ 1 - \left( 1 - \frac{x^2}{x_0^2} \right)^{\frac{3}{2}} \right] - 1 = 0.$$
 (7.2)

The first equation has one solution for  $1 < x_0 < \sqrt{\frac{3}{2}}$ , and the second equation has one solution when  $0 < x_0 < \sqrt{\frac{3}{2}}$ . Now, let us consider the case  $x > x_0$ . In this case, we have the point mass case and the equations would be:

$$1 - \frac{1}{x^2} = 0, (7.3)$$

$$1 - \frac{1}{x^2} = 0,$$

$$1 + \frac{1}{x^2} = 0.$$
(7.3)

In this case, it is obvious that (7.3) has one solution x = 1 and (7.4) has no solutions. The conclusion from this is that for  $0 < x_0 < 1$ , there are two critical curves which are circles whose radii are the solutions of (7.2) and (7.3); and, for  $1 < x_0 < \sqrt{\frac{3}{2}}$ , there are also two critical curves, which correspond to circles whose radii are the solutions of (7.1) and (7.2). Figure 4 shows these results.

In Figure 5, there is also an odd number of images. The images stopped being connected once the source is not on the origin of the mass distribution. Another interesting result is that the number of images goes from five to three in Figure 5 (columns 1 and 2). This is yet another common result from gravitational lensing.

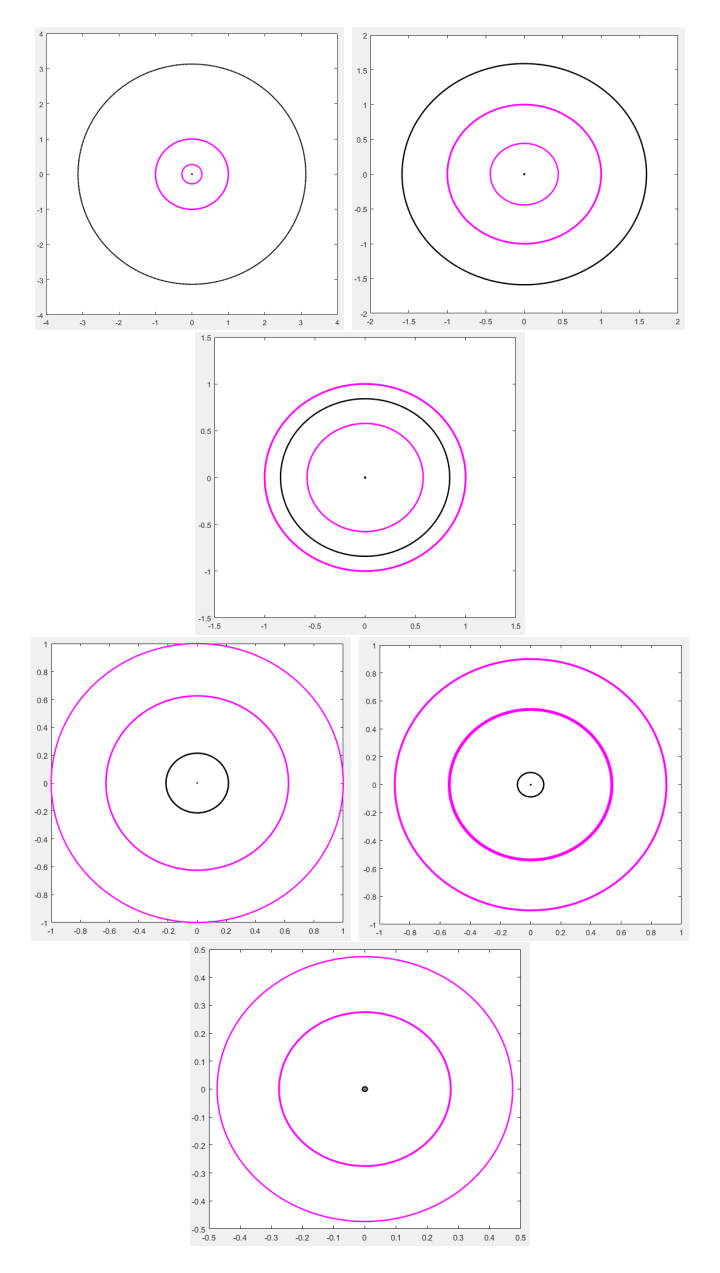


Figure 4: Caustics and critical curves for the uniform transparent sphere, for M = I. The critical curves are in magenta and the caustics in black. The top row has respectively, from left to right,  $x_0 = \{0.3, 0.5, 0.7\}$ . The bottom row has values, from left to right, of  $x_0 = \{1, 1.1, 1.2\}$ .

If the source crosses the caustic, the number of images is reduced by two [30]. In Figure 5, the caustic crossing can be seen.

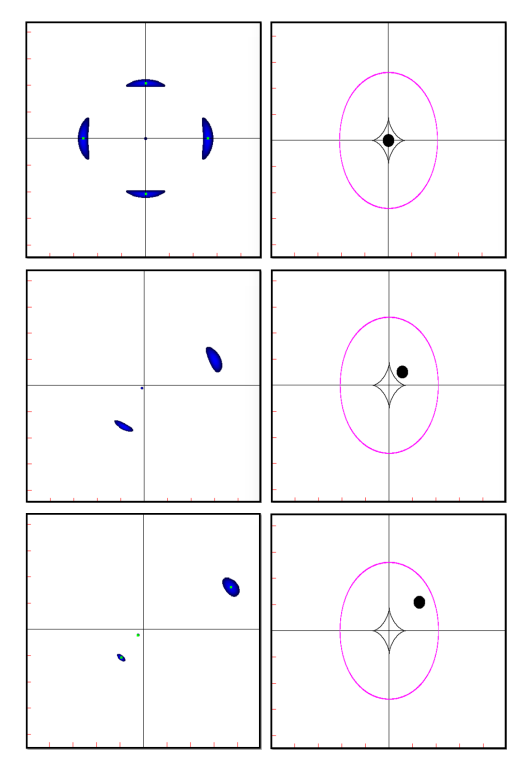
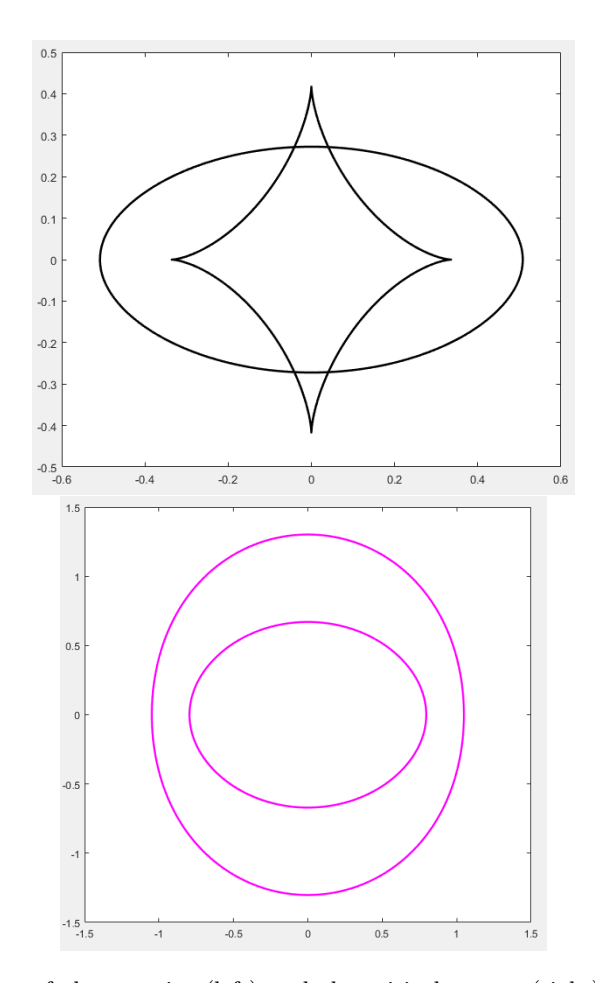


Figure 5: Images (left) and critical curves and caustics (right) for the uniform transparent sphere. The black dot represents where the original source is with respect to the center of the distribution, and the green dots represent individual images. The values for the parameters are:  $\sigma = 0.25$ ,  $\phi = 0$  and  $\gamma = 0.12$  and  $x_0 = 1$ .

The images shown in Figure 6 are the critical curve and caustic if  $x_0 = 1$ . The difference here is that both the diamond and the ellipse form as caustic solutions, and in the critical curves, two ellipse-like curves are forming as solutions.

From Figure 7, we have a particularly interesting result, because the central image that appeared in the other models does not appear in this case. The reason this occurs is that the central image is the result of the unlensed light from the source going perpendicularly through the lens and to the observer. However, the SIS model has a divergence in r=0 that results in the equation not giving this particular solution. This is consistent with the theory that predict an odd number of images, because these articles started from the assumption that the mass distribution was physically sensible, and that it did not have a divergence at the origin.



**Figure 6:** Images of the caustics (left) and the critical curves (right) plotted for the uniform transparent sphere. The parameters are  $\phi = 0$ ,  $\sigma = 0.25$ ,  $\gamma = 0.16$ . and  $x_0 = 1$ .

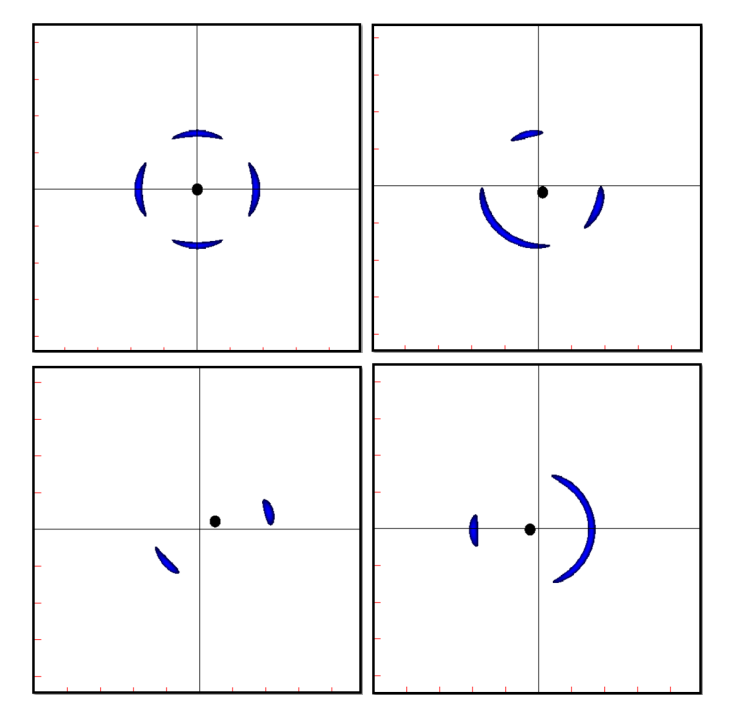
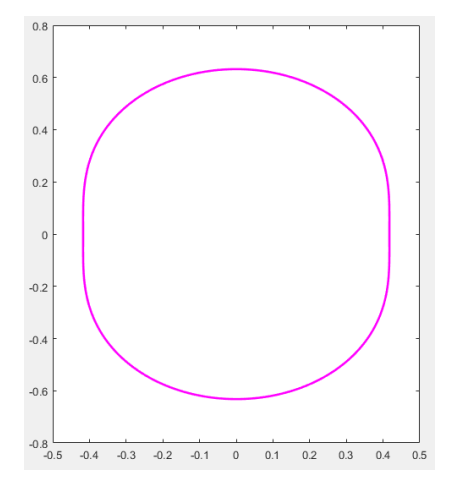
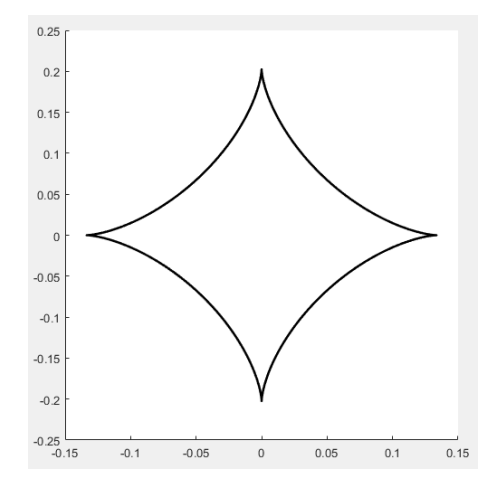


Figure 7: Lens images formed by a SIS distribution. The black dot represents where the original source is with respect to the center of the distribution. The parameters are  $\phi = 0$ ,  $\sigma = 0.16$  and  $\gamma = 0.12$ .

In 1980, Dyer and Roeder mentioned that they deduced the odd number of images for a transparent profile assuming that the matter distribution diverges less rapidly than 1/r as r goes to 0, which is not the case for the SIS profile [9]. What we observe in the images on figure 7 correspond to those that come in pairs in the transparent case, and not the one that goes from the source directly to the observer.

In Figure 8, it can be seen that the caustic solution for the transparent SIS profile is a diamond, and the critical curve it is an ellipse. These are very common as shapes for caustics and critical curves, even though they are not the only possible solutions. The NIS case is presented in Figure 9. In this case, four symmetrical images instead of an Einstein ring are observed, and the image from the center that goes through the matter distribution, because the lens is transparent. This is known as an Einstein cross, and it has been observed [30]. Five images appear in the top row and in the bottom left image, when one considers that the arc contains 3 images. In the bottom right image, the source is outside the distribution, resulting in two images from the point case.





**Figure 8:** Images of the caustics (left) and the critical curves (right) plotted for the Transparent SIS. The parameters are  $\phi = 0$ ,  $\sigma = 0.25$ ,  $\gamma = 0.16$  and  $x_0 = 1$ .

In Figure 10, the caustic and critical curves for NIS are quite different from the singular case. The graph for the caustic has a diamond-like figure, and the plot for the critic curve has a lemniscate-like figure.

The same interesting phenomenon as in the uniform transparent sphere is shown in Figures 11 and 12. There are two critical curves and two caustics. As in the transparent NIS profile, if the source is at the origin, an Einstein cross is observed. Another phenomenom, we can observe from Figure 11 is that, changing the values  $\gamma$ ,  $\phi$ ,  $\sigma$  of M the specific shape for the Einstein cross can change to the point it is no longer symmetric. Different values for these parameters can be adjusted so that a real image can be mapped with a model.  $\phi$  has the effect of rotating the images in this case. In Figure 11, we can also observe the transition from five to three and then to one image. Note that in the bottom left image, the arc embodies two images.

# 8. Conclusions

In this contribution, we present an extensive explanation regarding macro-gravitational lenses and how to calculate different properties of this images in the case of a transparent distribution of matter, following a specific profile.

With the help of XFGLenses, and with MATLAB, we show different images that arise from all of these profiles, and the different caustics and critical curves. The images are consistent with several previous results that are expected for transparent profiles. One of them is that these give rise to an odd number of images [9, 24], even though, as stated before, this may not be a necessary condition [13].

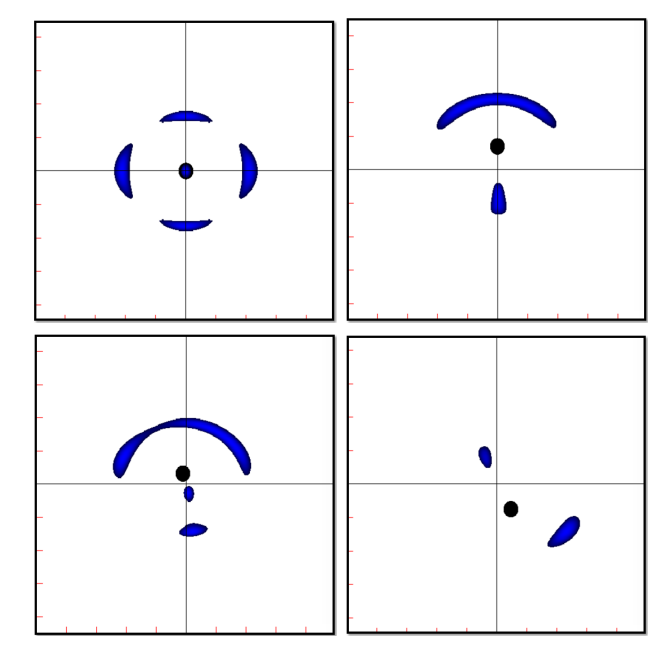
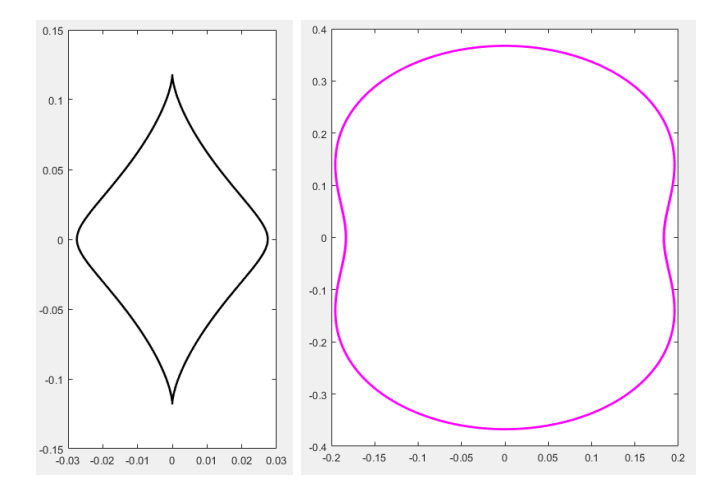


Figure 9: Lens images formed by a NIS distribution. The black dot represents where the original source is with respect to the center of the distribution. The parameters are  $\phi = 0$ ,  $\sigma = 0.33$  and  $\gamma = 0.16$ .



**Figure 10:** Images of the caustics (left) and the critical curves (right) plotted for the transparent NIS. The parameters are  $\phi = 0$ ,  $\sigma = 0.25$ ,  $\gamma = 0.16$  and  $x_0 = 1$ .

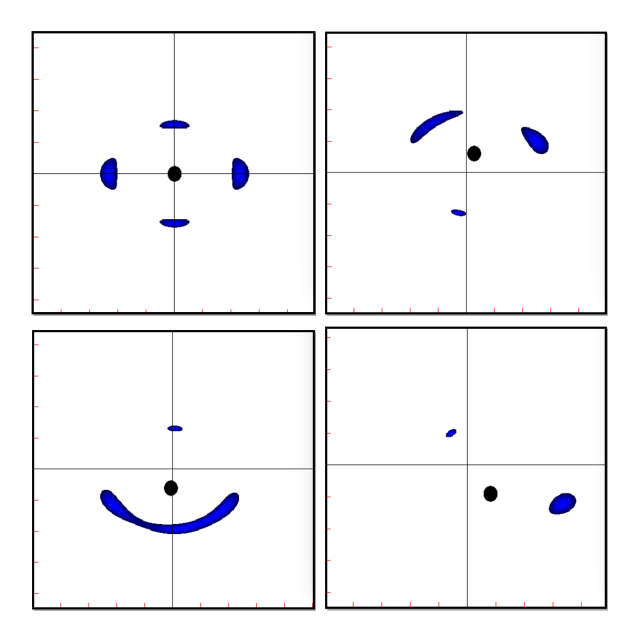


Figure 11: Lens images formed by a transparent King distribution. The black dot represents where the original source is with respect to the center of the distribution. In the 4 images,  $\phi = 0$ . For  $\gamma$ , in the first row and bottom left image  $\gamma = 0.16$  and in the bottom right  $\gamma = 0.08$ . For  $\sigma$ , the first column have  $\sigma = 0.33$  and the second column  $\sigma = 0.25$ . In the Einstein cross, the central image is little and opaqued by the source.

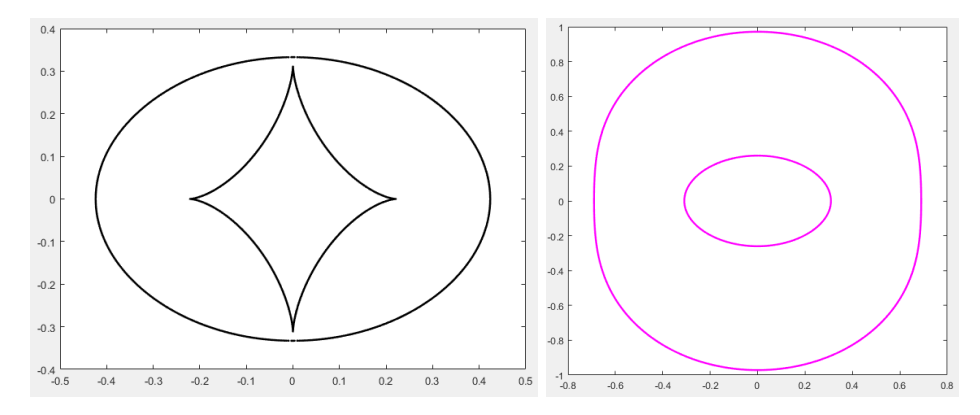


Figure 12: Images of the caustics (left) and the critical curves (right) plotted for the transparent King. The parameters are  $\phi = 0$ ,  $\sigma = 0.25$ ,  $\gamma = 0.16$  and  $x_0 = 1$ .

The other one is that if the sources passes through the caustic, the number of images is reduced by two [30]. These images are also consistent with some of the lenses from previous observations ([17, 28, 32]). Finally, the curves shown in the caustics where the diamond, the ellipse and the lemniscate-like. For the critical curves, the most common curve is the ellipse, and the lemniscate-like appear in the transparent NIS case, which is consistent with the fact that these curves are common in gravitational lens theory.

#### 9. Acknowledgements and Funding

We would like to thank the Vice Rectory of Research and the School of Physics at the University of Costa Rica, whose support has been fundamental to our research.

## References

- [1] R. J. Adler, W. C. Barber, M. E. Redar, *Gravitational lenses and plastic simulators*. American Journal of Physics **63**(1995), no. 6, 536–541. DOI: 10. 1119/1.17865
- A. Barnacka, Gravitational lenses as high-resolution telescopes. Physics Reports 778-779 (2018). Gravitational lenses as high-resolution telescopes, 1–46.
   DOI: 10.1016/j.physrep.2018.10.001
- [3] R. R. Bourassa, R. Kantowski, *The theory of transparent gravitational lenses*. The Astrophysical Journal **195**(1975), 13. DOI: 10.1086/153300
- [4] R. R. Bourassa, R. Kantowski, T. D. Norton, The Spheroidal Gravitational Lens. The Astrophysical Journal 185(1973), 747. DOI: 10.1086/152452
- I. Bray, Spheroidal gravitational lenses. Monthly Notices of the Royal Astronomical Society 208(1984), 511–516. DOI: 10.1093/mnras/208.3.511
- [6] O. Chwolson, Über eine mögliche Form fiktiver Doppelsterne. Astronomische Nachrichten **221**(1924), no. 20, 329–330. DOI: 10.1002/asna.19242212003
- [7] E. E. Clark, The Uniform Transparent Gravitational Lens. Monthly Notices of the Royal Astronomical Society 158(1972), no. 2, 233–243. DOI: 10.1093/mnras/158.2.233
- [8] J. P. Coles, J. I. Read, P. Saha, Gravitational lens recovery with glass: measuring the mass profile and shape of a lens. Monthly Notices of the Royal Astronomical Society 445(2014), no. 3, 2181–2197. DOI: 10.1093/mnras/stu1781
- [9] C. C. Dyer, R. C. Roeder, Possible multiple imaging by spherical galaxies.
   The Astrophysical Journal 238(1980), L67. DOI: 10.1086/183260
- [10] M. Falbo-Kenkel, J. Lohre, Simple gravitational lens demonstrations. The Physics Teacher 34(1996), no. 9, 555–557. DOI: 10.1119/1.2344566
- [11] F. Frutos-Alfaro, A computer program to visualize gravitational lenses. American Journal of Physics **69**(2001), no. 2, 218–222. DOI: 10.1119/1.1290251

- [12] F. Frutos-Alfaro, Reduction of the gravitational lens equation to a one-dimensional non-linear form for the tilted Plummer model family. Monthly Notices of the Royal Astronomical Society: Letters 376(2007), no. 1, L72–L75. DOI: 10.1111/j.1745-3933.2007.00289.x
- [13] D. H. Gottlieb, A gravitational lens need not produce an odd number of images. Journal of Mathematical Physics **35**(1994), no. 10, 5507–5510. DOI: 10.1063/1.530762
- [14] J. Higbie, Gravitational lens. American Journal of Physics 49(1981), no. 7, 652–655. DOI: 10.1119/1.12440
- [15] G. Hinshaw, L. M. Krauss, Gravitational Lensing by Isothermal Spheres with Finite Core Radii: Galaxies and Dark Matter. Astrophysical Journal 320(1987), 468. DOI: 10.1086/165564
- [16] V. Icke, Construction of a gravitational lens. American Journal of Physics 48(1980), no. 10, 883–886. DOI: 10.1119/1.12284
- [17] C. Jacobs et al., An Extended Catalog of Galaxy–Galaxy Strong Gravitational Lenses Discovered in DES Using Convolutional Neural Networks. The Astrophysical Journal Supplement Series 243(2019), no. 1, 17. DOI: 10.3847/1538-4365/ab26b6
- [18] R. Kantowski, B. Chen, X. Dai, Fermat's least-time principle and the embedded transparent lens. Phys. Rev. D 88(2013) 8, 083001. DOI: 10.1103/PhysRevD.88.083001
- [19] H. Karttunen et al., Fundamental astronomy. Springer, 2007. DOI: 10.1007/ 978-3-540-34144-4
- [20] R. Kayser, P. Helbig, T. Schramm, A general and practical method for calculating cosmological distances. 1997. DOI: 10.48550/arXiv.astro-ph/9603028
- [21] I. R. King, Density Data and Emission Measure for a Model of the Coma Cluster. The Astrophysical Journal 174(1972), L123. DOI: 10.1086/180963
- [22] S. Liebes, Gravitational Lenses. Physical Review 133(1964), no. 3B, B835–B844. DOI: 10.1103/physrev.133.b835
- [23] S. Liebes, *Gravitational Lens Simulator*. American Journal of Physics **37**(1969), no. 1, 103–104. DOI: 10.1119/1.1975345
- [24] R. H. McKenzie, A gravitational lens produces an odd number of images. Journal of Mathematical Physics 26(1985), no. 7, 1592–1596. DOI: 10.1063/ 1.526923
- [25] M. J. Nandor, T. M. Helliwell, Fermat's principle and multiple imaging by gravitational lenses. American Journal of Physics 64(1996), 45–49. DOI: 10. 1119/1.18291
- [26] P. R. Newbury, R. J. Spiteri, *Inverting Gravitational Lenses*. SIAM Review 44(2002), no. 1, 111–130. DOI: 10.1137/S0036144500380934

- [27] B. Patla, R. J. Nemiroff, Gravitational Lensing Characteristics of the Transparent Sun. The Astrophysical Journal 685(2008), no. 2, 1297. DOI: 10.1086/588805
- [28] M. Quirós-Rojas et al., ALMA follow-up of 3000 red-Herschel galaxies: the nature of extreme submillimetre galaxies. Monthly Notices of the Royal Astronomical Society 533(2024), no. 3, 2966–2979. DOI: 10.1093/mnras/stae1974
- [29] T. Sauer, Nova Geminorum 1912 and the Origin of the Idea of Gravitational Lensing. Archive for History of Exact Sciences 62(2008), 1–22. DOI: 10.1007/ s00407-007-0008-4
- [30] P. Schneider, J. Ehlers, E. E. Falco, Gravitational Lenses. Springer Berlin Heidelberg, 1992. DOI: 10.1007/978-3-662-03758-4
- [31] M. Selmke, An optical n-body gravitational lens analogy. American Journal of Physics 89(2021), no. 1, 11–20. DOI: 10.1119/10.0002117
- [32] A. Sonnenfeld et al., Survey of Gravitationally-lensed Objects in HSC Imaging (SuGOHI). I. Automatic search for galaxy-scale strong lenses. Publications of the Astronomical Society of Japan 70(2017), no. SP1, S29. DOI: 10.1093/pasj/psx062
- [33] B. Szafraniec, J. F. Harford, A simple model of a gravitational lens from geometric optics. American Journal of Physics 92(2024), no. 11, 878–884. DOI: 10.1119/5.0157513
- [34] H. Thuruthipilly, A. Zadrozny, A. Pollo, M. Biesiada, Finding strong gravitational lenses through self-attention Study based on the Bologna Lens Challenge. A&A 664(2022), A4. DOI: 10.1051/0004-6361/202142463
- [35] E. L. Turner, J. P. Ostriker, J. R. Gott III, The statistics of gravitational lenses: the distributions of image angular separations and lens redshifts. Astrophysical Journal 284(1984), 1–22. DOI: 10.1086/162379
- [36] P. van Dokkum et al., A massive compact quiescent galaxy at z=2 with a complete Einstein ring in JWST imaging. Nature Astronomy 8(2024), 119. DOI: 10.1038/s41550-023-02103-9
- [37] D. Walsh, R. Carswell, R. Weymann, 0957+561 A, B: Twin quasistellar objects or gravitational lens? Nature 279(1979), 381–384. DOI: 10.1038/ 279381a0
- [38] S. Xu, G. Su, Y. Zhang, Y. Liu, Mimicking gravitational lens on a thin elastic plate. Applied Physics Letters 120(2022), no. 3, 031106. DOI: 10.1063/5. 0075683
- [39] P. Young et al., The double quasar Q0957+561 A, B: a gravitational lens image formed by a galaxy at z=0.39. Astrophysical Journal 241(1980), 507– 520. DOI: 10.1086/158365